New Journal of Physics
The open access journal at the forefront of physics

Deutsche Physikalische Gesellschaft DPG
IOP Institute of Physics

Published in partnership with: Deutsche Physikalische Gesellschaft and the Institute of Physics

OPEN ACCESS

RECEIVED
9 May 2017

REVISED
18 July 2017

ACCEPTED FOR PUBLICATION
3 August 2017

PUBLISHED
7 December 2017

PAPER

Sm cluster superlattice on graphene/Ir(111)

Dimitris Mousadakos, Marina Pivetta, Harald Brune and Stefano Rusponi

Institute of Physics, École Polytechnique Fédérale de Lausanne (EPFL), CH-1015 Lausanne, Switzerland

E-mail: stefano.rusponi@epfl.ch

Keywords: metal cluster superlattice, graphene, rare earths, nucleation and growth, scanning tunneling microscopy (STM)

Abstract

We report on the first example of a self-assembled rare earth cluster superlattice. As a template, we use the moiré pattern formed by graphene on Ir(111); its lattice constant of 2.52 nm defines the interparticle distance. The samarium cluster superlattice forms for substrate temperatures during deposition ranging from 80 to 110 K, and it is stable upon annealing to 140 K. By varying the samarium coverage, the mean cluster size can be increased up to 50 atoms, without affecting the long-range order. The spatial order and the width of the cluster size distribution match the best examples of metal cluster superlattices grown by atomic beam epitaxy on template surfaces.

1. Introduction

The fabrication of nanostructure superlattices has attracted a lot of attention in recent decades. Clusters of nanometric sizes display unique properties, neither seen in bulk nor in the individual atoms of the respective element [1]. In addition, the ability to create clusters with identical sizes and shapes, and to arrange them in ordered arrays has great importance for both fundamental research and for applications. For example, equidistant, monodisperse and equally oriented magnetic clusters have uniform magnetic moments and coercivity. Therefore, they are the best candidates for application in magnetic recording media of the future. Similarly, dense arrays of identical clusters are candidates for catalysts with improved performances.

One way of fabricating cluster arrays is the bottom-up approach by atomic beam epitaxy (ABE) in ultrahigh vacuum (UHV) conditions [2]. Atoms are evaporated onto a template surface, where they diffuse and nucleate clusters on preferential sites. In this way, periodic arrays of seeds form, reproducing the symmetry and the period imposed by the template [3–15]. Cluster size and shape can then be controlled to a certain extent by varying the amount of deposited atoms (coverage), the substrate temperature during deposition (T_{dep}) and the annealing temperature after deposition (T_{ann}). Long-range spatial order and narrow size distribution characterize the high quality arrays. Well known examples of templates for the assembly of metal cluster superlattices are the dislocation network that two layers of Ag form on Pt(111) to release the stress generated by the lattice mismatch [16], the reconstruction forming at the surface of Si(111) [17–19], Au(111) [20, 21] and the vicinal Au surfaces [6], the moiré patterns observed for graphene (gr) [9, 22, 23] and hexagonal BN (*h*-BN) [24, 25] grown on mismatched transition metal substrates, or the hexagonal array of holes in the alumina bilayer formed by high temperature oxidation of $Ni_3Al(111)$ [7, 26].

So far, only arrays of clusters made of transitional metals have been successfully grown on such templates, while the formation of rare earth superlattices has never been reported despite their potential in magnetic and catalytic applications. The large spin–orbit coupling of the highly localized *4f* orbitals of rare earths can lead to large magnetic anisotropy [27, 28] overcoming the values observed in *3d* metals [29, 30], thus allowing for magnetic remanence in very small clusters. For example, magnetic remanence has been recently reported for Er trimers at 3 K [31], while trimers made of *3d* elements (Fe) exhibit magnetic bistability only at 0.3 K [32]. Moreover, bimetallic clusters made of *4f-3d* metals may well show very large coercive fields, similarly to what is observed in bulk [33]. In catalysis, rare earth oxides show high selectivity in the formation or decomposition of numerous chemical compounds [34–38].

Here we demonstrate the self-assembly of a rare earth cluster superlattice by ABE using the graphene moiré pattern formed on Ir(111) as a template. Sm atoms order in cluster superlattices for deposition temperatures ranging from 80 K to 110 K. The interparticle distance of 2.52 nm is defined by the moiré period, with a single Sm cluster nucleated per moiré unit cell. The spatial order is preserved up to the Sm coverage yielding a mean cluster size of 50 atoms. The long-range order and the width of the cluster size distribution sets the Sm superlattice among the best examples of cluster arrays grown by ABE on template surfaces.

A similar study carried out with Dy reveals the absence of order. The observed cluster densities as a function of deposition temperature suggest that the adatom diffusion barrier of Dy is lower than that of Sm, in agreement with the calculations of diffusion barriers on free-standing graphene [39]. We attribute the formation (lack) of the Sm (Dy) superlattice to the delicate balance among the adatom diffusion barrier, the differences in adatom binding energies on the graphene moiré, and the Coulomb repulsion between the adatoms induced by a charge transfer from rare earth to graphene.

2. Results and discussion

We investigated the nucleation of Sm on gr/Ir(111) by measuring the island density as a function of deposition temperature T_{dep} for a Sm coverage $\Theta_{Sm} = 0.08$ monolayer (ML), with one ML corresponding to one rare earth atom per Ir(111) unit cell. Immediately after deposition, the sample temperature was lowered to 80% of the deposition temperature in order to freeze surface diffusion and avoid any post-deposition effects [40]. The sample morphology has been characterized by scanning tunnelling microscopy (STM), for more information see the appendix. The cluster density n_x, expressed in ML, is the number of islands per Ir(111) unit cell, and is shown in the Arrhenius plot in figure 1(a). Since the moiré pattern is a (9.32 × 9.32) superstructure with respect to Ir(111) [41], one cluster per moiré unit cell corresponds to $n_x = 1.15 \times 10^{-2}$ ML, or $\log n_x = -1.94$.

When compared with the STM images shown in figures 1(b)–(f), one can distinguish four regimes. The first starts at the lowest investigated T_{dep} of 56 K and goes up to 78 K. The clusters are disordered, see figure 1(b), and their density is higher than the moiré cell density. The second regime, ranging from 80 K up to 110 K, exhibits an excellent order with one cluster per unit cell and these clusters are placed at identical sites within the moiré unit cell, see figure 1(c). We attribute the fact that n_x is slightly smaller than one island per moiré unit cell to graphene defects that give rise to empty cells which can also be identified in figure 1(c). Above 110 K we enter in a third regime where the order is lost, but the mean density stays at around one island per moiré unit cell, see figure 1(d). Above 130 K, the density sharply decreases and then reaches another stationary value for T_{dep} up to 200 K, figure 1(e). Finally, the fourth regime is characterized by a progressive Sm intercalation with almost full intercalation taking place for $T_{dep} = 280$ K, see figure 1(f). At this temperature, the intercalated atoms move over large distances to form extended islands, as for Eu on gr/Ir(111) [42].

To quantify the degree of spatial order and characterize the order-disorder transitions as a function of the deposition temperature, we use a procedure proposed for superlattices of 3D nanocrystals [43]. It is based on the quantitative analysis of the radial decay of the 2D-autocorrelation function (2D-ACF) derived from the TEM and, in the present case, the STM images. As we will see below, this allows us to quantify the differences between superlattices that appear to be of a very similar quality to the eye. The 2D-ACF exhibits its global maximum in the image center ($r = 0$) and, for ordered systems, satellite maxima which lie along the high symmetry directions of the superlattice. The position of these satellite maxima corresponds to the superlattice period. Their intensity is correlated with the degree of order including periodicity of the unit cells as well as uniformity of the shape and center of the mass of the motif. To exemplify the analysis procedure, we show in figure 2(a) the STM image of a Sm cluster superlattice grown at 100 K and, in figure 2(b), the corresponding 2D-ACF. The radial profile of the 2D-ACF is shown in figure 2(c). Its envelope is fitted by the following function:

$$env(r) = A_\infty + f_0 \exp\left(-\frac{1}{2}(r/\sigma_0)^2\right) + f \exp\left(-\frac{1}{2}(r/\sigma)^2\right). \quad (1)$$

A_∞ is the asymptotic height of the satellite peaks as r goes to infinity. The first Gaussian term describes the central peak of the 2D-ACF. The height f_0 of this peak is related to the sample roughness [44–46] and is therefore sensitive to non-uniformities in cluster shapes, height and random voids, such as empty cells in our case. Apparent height variations due to modifications of the tip shape from image to image also contribute to the spreading of the f_0 values. The width σ_0 is usually set to one third of the mean interparticle distance [43], in our case $\sigma_0 = 0.83$ nm. f and σ in the second Gaussian, together with A_∞, are the parameters characterizing the long-range order of the superlattice. Small f and high A_∞ values indicate good long-range order. Two figures of merit, ξ and κ, have been introduced to quantify the superlattice quality [43]:

$$\xi = A_\infty/(f + A_\infty) \quad (2)$$

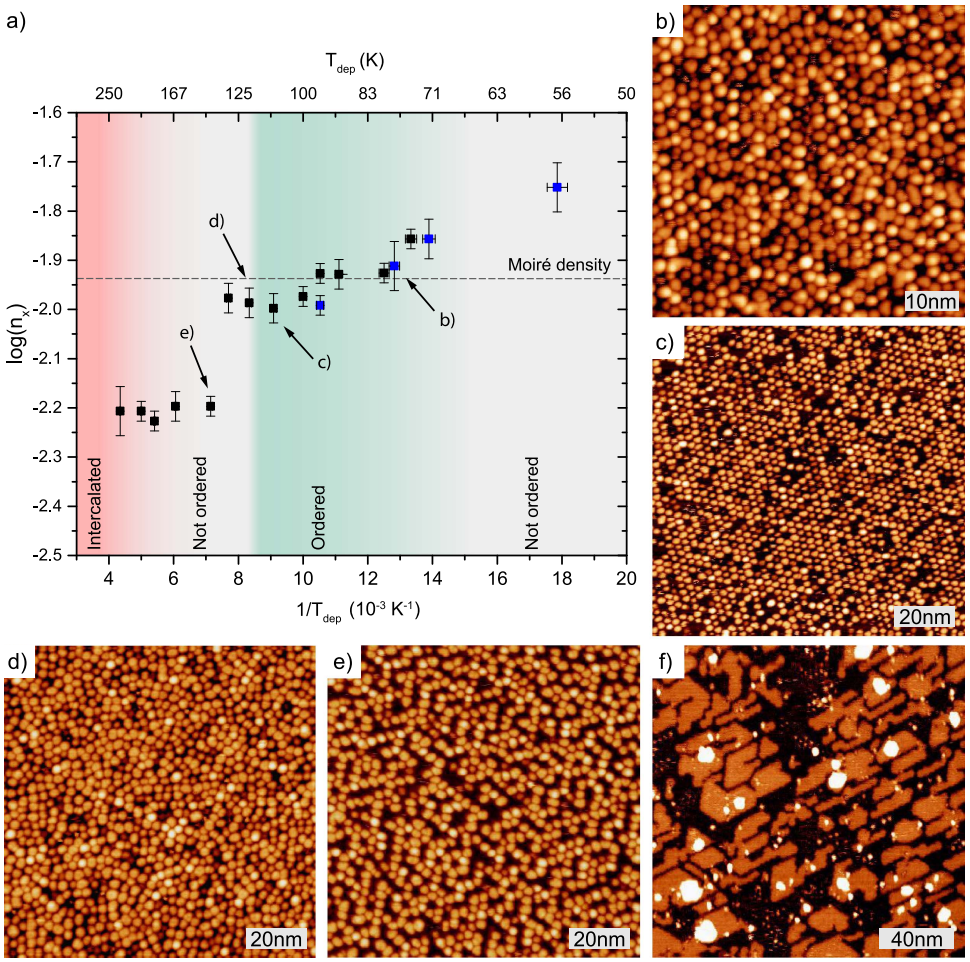

Figure 1. (a) Arrhenius plot of the Sm cluster density as a function of T_{dep}. Black squares indicate VT-STM measurements and blue ones data taken with a 4 K STM (see the appendix). (b-e) STM images of Sm clusters on gr/Ir(111) for $\Theta_{Sm} = 0.08$ ML. (b) $T_{dep} = 78$ K, disordered regime ($V_t = +1.0$ V, $I_t = 50$ pA). (c) $T_{dep} = 110$ K, one cluster per moiré unit cell and these clusters are situated at identical positions within the moiré, graphene defects are causing some empty cells ($V_t = -1.3$ V, $I_t = 75$ pA). (d) $T_{dep} = 120$ K, the density stays constant but the order is lost ($V_t = -0.7$ V, $I_t = 50$ pA). (e) $T_{dep} = 140$ K, density is below one island per moiré unit cell ($V_t = -0.6$ V, $I_t = 50$ pA). (f) $T_{dep} = 280$ K, $\Theta_{Sm} = 0.16$ ML, intercalated islands (orange), appearance of clusters (white) in the second layer ($V_t = -1.1$ V, $I_t = 60$ pA).

$$\kappa = \sigma(f + A_\infty)/f \tag{3}$$

ξ ranges from 1 for perfect superlattices to 0 for completely disordered systems and expresses the degree of long-range order by quantifying the decay of $env(r)$ amplitude. κ indicates over which distance this decay takes place as it contains the width of the second Gaussian. However, this parameter gives useful information in addition to ξ only for ordered systems, since κ may well be high in disordered samples where both f and A_∞ are small.

For the Sm superlattice, a long-range order is observed for T_{dep} ranging between 80 K and 110 K, with 100 K giving the highest value of $\xi = 0.75$, as shown in figure 2(d). In this regime, κ is larger than 30 nm. From the 1D profile of the ACF, we deduce an interparticle distance of (2.52 ± 0.02) nm, demonstrating that the clusters nucleate in registry with the moiré pattern. The very large apparent size of the Sm clusters, imaged as occupying almost the entire moiré unit cell, hampers a clear identification of the adsorption site. Assuming an identical adsorption site for the clusters as the one observed for Dy single atoms [49], the atop region in the moiré unit cell [9] would be the preferential site. The main sources of disorder are the vacancies, their number is $12 \pm 2\%$ of the moiré cells. Outside the 80 K–110 K temperature range, ξ decreases below 0.2.

Having introduced the above figures of merit, in table 1 we compare the degree of the long-range order of the Sm cluster superlattice with self-assembled island superlattices reported in the literature. With $\xi = 0.75$, Sm/gr/Ir(111) is among the ones with the best long-range order. The only other system implying rare earth atoms are Eu clusters on gr/Ir(111) [42]. It is characterized by $\xi = 0.32$ and thus its long-range order is significantly lower. We underline that some superlattices characterized by a uniform island size show low ξ owing to irregular island shapes and to the randomly shifted position of the island center of mass with respect to a defined location in the cell.

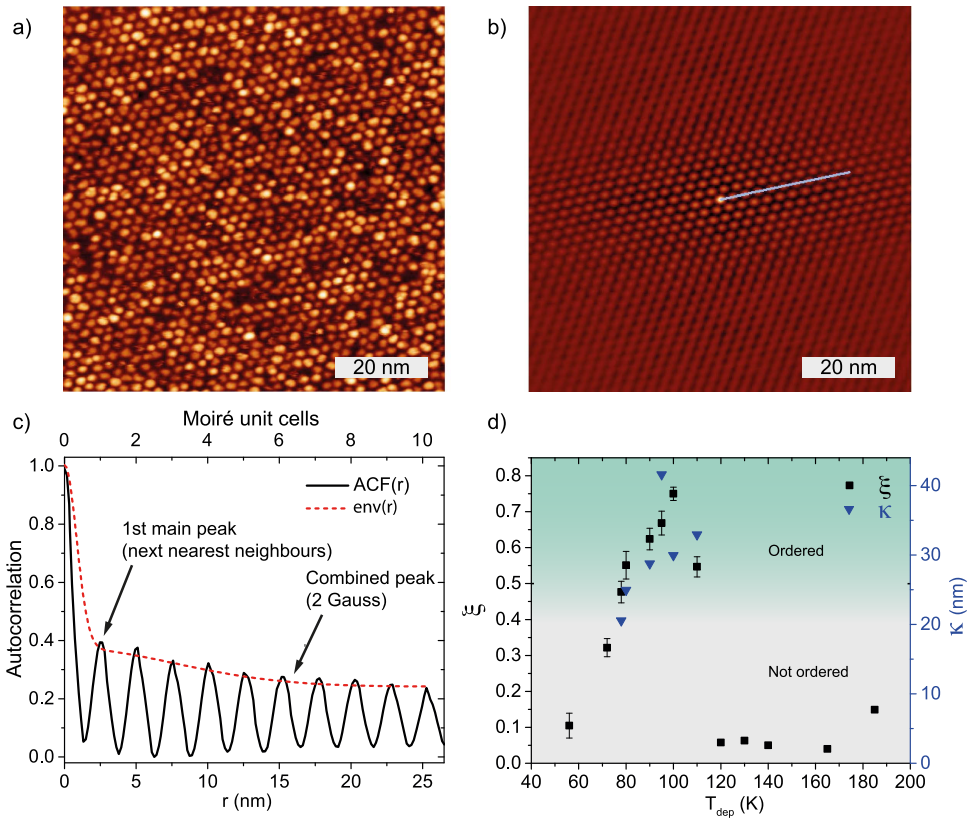

Figure 2. (a) STM image of Sm clusters grown at $T_{dep} = 100$ K ($V_t = -1.1$ V, $I_t = 60$ pA). (b) 2D-ACF of the image (a); the vertical direction is the slow scan direction and exhibits less order as it is more affected by distortions due to thermal drift. (c) Line-profile along a high symmetry direction of the 2D-ACF in (b) and of the envelope fit with equation 1 (dashed red line). (d) Figures of merit ξ and κ characterizing the order as a function of the deposition temperature.

The long-range order of the Sm cluster superlattice is preserved up to a coverage of about $\Theta_{Sm} = 0.5$ ML. For samples grown at $T_{dep} = 90$ K, ξ only slightly decreases from 0.62 ($\Theta_{Sm} = 0.08$ ML) to 0.56 ($\Theta_{Sm} = 0.5$ ML) and κ from 30.6 to 18.4 nm, respectively. For coverages above 0.5 ML the clusters start to coalesce.

In addition to the long-range order, a second parameter defining the quality of a cluster superlattice is the width of the cluster size distribution. For 0.08 ML of Sm deposited at 110 K, this distribution is shown in the inset of figure 3 together with a Gaussian fit (see the appendix for the size distribution analysis). The half width at half maximum (HWHM) of the size distribution is $\sigma_{SD} = 0.31 \pm 0.01$. This value is roughly half the one $\sigma_{SD} = 0.59$ expected for a homogeneous nucleation [2], equals the widths observed for several superlattices grown on template surfaces [9, 15, 50–54] and is very close to the best result of $\sigma_{SD} = 0.20$ [4, 8]. We note that a narrower size distribution with $\sigma_{SD} \approx 0.15$ has been reported for magic clusters of Ga [55] or Al [18] on Si(111)-7 × 7. However, this result applies exclusively to clusters consisting of 6 atoms (magic size). For the present system, two main factors contribute to the width of the size (s) distribution. The first is the cluster coalescence which takes place above $s/S = 3.2$, where S is the mean island size, and affects 4 ± 1% of the islands. The second is the non-uniform island height, with 90 ± 2% of the islands being mono-layered and the remaining ones being bi-layered.

We investigated the thermal stability of the Sm superlattice by measuring the cluster density as a function of the annealing temperature T_{ann} (see figure 3). The density remains constant up to 140 K, from which it reduces exponentially, leading to a progressive loss of order. This onset temperature can be related to the cluster–graphene interaction. On gr/Ir(111), clusters of similar sizes (coverage < 0.25 ML) show an onset temperature for the coarsening of 160 K for Au, and of 550 K for Pt and Ir [11]. The high thermal stability observed for Pt and Ir is a consequence of the covalent bonds formed between the atoms in the cluster and the graphene layer, forcing an sp^2 to sp^3 re-hybridization of C [56], while a weaker bond is expected for Au due to its completely filled 5d-shell [11]. The low onset temperature observed for Sm, even lower than for Au, suggests a weak Sm–graphene bond.

In order to investigate whether the superlattice formation is a general property of rare earth elements on graphene/Ir(111) or specific to Sm, we carried out similar experiments with Dy. For deposition temperatures

Table 1. Figures of merit characterizing the long-range order for different cluster superlattices grown by ABE on template surfaces. ξ and κ are calculated from the published data. κ in units of the pitch are rounded to the nearest integer. For vicinal surfaces, ξ and κ have been evaluated along and perpendicular to the steps, and for the Au(111)-($\sqrt{3} \times 22$), reconstructed along the [1 $\bar{1}$ 2] direction. For superlattices with $\xi < 0.4$, κ is not representative of the long-range order extension.

	System	ξ	κ (nm)	Pitch (nm)	κ (pitch)	T_{dep} (K)
4f	Sm/gr/Ir(111)[a d]	0.75	31.8	2.53	13	100
	Eu/gr/Ir(111)[b] [42]	0.32	—	2.53	—	35
	Dy/gr/Ir(111)[a d]	0.27	—	2.53	—	70
3d	Rh/gr/Ir(111)[e] [14]	0.87	40.4	2.53	16	130
	Co/Au(788) [$\bar{2}$ 1 1] [8]	0.76	55.8	3.5	16	130
	Pt/gr/Ir(111)[b] [11]	0.76	22.3	2.53	9	300
	Ir/gr/Ir(111)[b] [9]	0.75	28.4	2.53	11	300
	Rh/gr/Ir(111)[a e]	0.73	39.7	2.53	16	110
	Fe/2 ML Cu/Pt(111) [4]	0.73	24.6	4.8	5	250
	Al/Si(111)[c] [18]	0.73	21.8	2.69	8	473
	Ir/gr/Ir(111)[a] [12]	0.67	12.1	2.53	5	300
	Co/GdAu$_2$/Au(111) [15]	0.62	19.1	3.8	5	300
	Mn/Si(111) [19]	0.61	26.6	2.69	10	353
	Co/Au(11,12,12) [0 1 $\bar{1}$] [6]	0.61	20.2	7.2	3	300
	Co/Au(788) [0 1 $\bar{1}$] [8]	0.51	32.4	7.2	5	130
	Ag/2 ML Ag/Pt(111) [4]	0.46	17.7	7.0	3	110
	Co/*h*-BN/Rh(111) [10]	0.46	11.6	3.2	4	4.2
	Pd/Al$_2$O$_3$/Ni$_3$Al(111) [7]	0.44	26.7	4.5	6	300
	Fe/(NC-Ph$_5$-CN)$_3$Cu$_2$/Cu(111) [13]	0.43	43.8	5.0	9	10+ann.
	Fe/Au(111) [1 $\bar{1}$ 2] [47]	0.37	—	7.3	—	300
	Co/Au(111) [1 $\bar{1}$ 2] [3]	0.35	—	7.3	—	300
	Ni/Au(111) [1 $\bar{1}$ 2] [48]	0.32	—	7.3	—	300

[a] Full graphene layer.
[b] Graphene patches.
[c] Honeycomb lattice.
[d] Present work.
[e] Unpublished results.

ranging from 47 K to 210 K ($\Theta_{Dy} = 0.07$ ML), we did not observe the formation of cluster arrays. A cluster density close to the graphene moiré density is found for $T_{dep} = 70$ K, see figure 4(a), which is lower than the 80 K measured for Sm. This observation suggests a lower diffusion barrier for Dy compared to Sm, in agreement with theoretical calculations on the free-standing graphene [39], which represent a good approximation given the weak interaction between graphene and Ir(111) [57]. Additionally, we observe that intercalation starts at a temperature lower than Sm, namely at about 210 K. Figure 4(b) shows an STM image and the corresponding 2D-ACF of a sample grown at 70 K. The quantitative analysis gives $\xi = 0.27$. The absence of order suggests that the adatom diffusion barrier and the corrugation of the graphene moiré potential are not the only parameters responsible for the superlattice formation. A third ingredient is the Coulomb repulsion between rare earth adatoms induced by the charge transfer from adatoms to graphene [39, 42, 58]. Depending on the temperature, this repulsion hampers nucleation and leads to the formation of a 2D adatom gas from which clusters may nucleate by direct impingement of the incoming atoms on top of the adatoms. This nucleation channel competing with lateral attachment leads to disorder. This suggests that a certain balance between the adatom diffusion barrier, graphene moiré potential, and the adatom–adatom Coulomb repulsion is required for the superlattice formation.

3. Conclusion

We have studied the nucleation of Sm and Dy on the moiré pattern formed by gr/Ir(111). We observe the formation of a cluster superlattice for Sm deposition between 80 K and 110 K, whereas Dy clusters are disordered for all investigated deposition temperatures. The long-range order of the Sm superlattice has been evaluated in comparison with examples of transition metal cluster arrays from the literature. The present case is the first well-ordered, self-assembled superlattice for a *4f* element. Its long-range order is competitive to the best results obtained for transition metals. The Sm cluster size distribution has a Gaussian shape with $\sigma_{SD} = 0.31 \pm 0.01$ nm. Superlattices of Sm clusters with an average size of nine atoms lose the order by

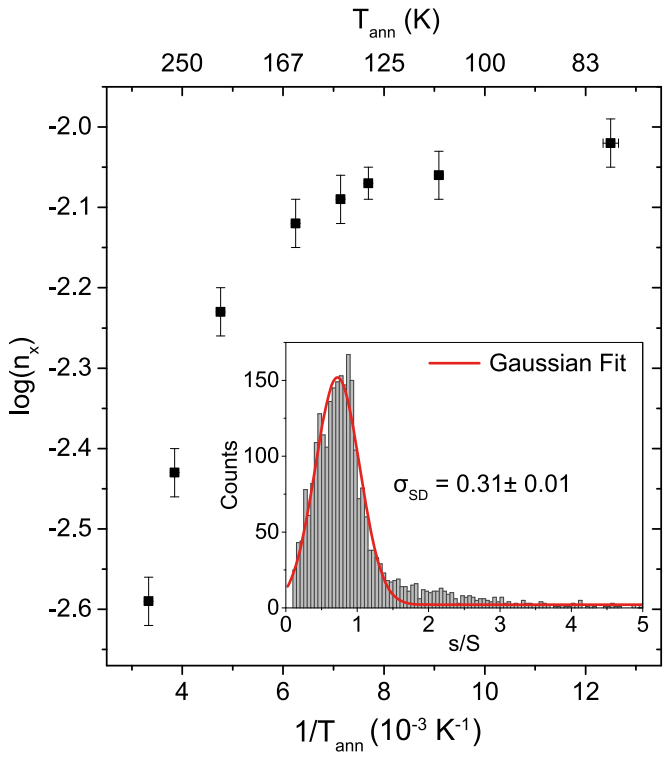

Figure 3. Arrhenius plot of the cluster density n_x as a function of T_{ann} after depositing $\Theta_{Sm} = 0.08$ ML at $T_{dep} = 80$ K. Inset: Sm cluster size (s) distribution for the as grown sample at $T_{dep} = 110$ K. The average cluster size is $S = 9$ atoms.

annealing at 140 K, suggesting a weak Sm–graphene bonding. The Sm superlattice formation opens the possibility to grow periodic arrays of two-element clusters, for example $SmCo_5$, which is one of the strongest magnets discovered so far, without the need of an additional seeding element.

Acknowledgments

We gratefully acknowledge funding by the Swiss National Science Foundation (Grant No. 200020_157081/1).

Appendix. Sample preparation and measurement details

The experiments have been performed in two ultrahigh vacuum (UHV) chambers. The first has a base pressure of 6×10^{-11} mbar and is equipped with a variable temperature STM (VT-STM) operating down to 70 K and a magneto-optical Kerr effect (MOKE) setup with all optical components in vacuum [54]. The second has a a base pressure of 5×10^{-11} mbar and houses a low temperature STM operating down to 5 K [59]. The Ir(111) crystals were prepared in both systems by cycles of Ar^+ ion sputtering (0.9 keV, 2 $\mu A/cm^2$) at room temperature and at 1120 K, followed by annealing at 1500 K. The graphene layer was grown on Ir(111) by exposing the crystal surface at a temperature of 1400 K to 100 Langmuir of ethylene [41, 60]. At this temperature the hydrocarbons decompose when interacting with the surface, H desorbs leaving only the carbon atoms to form the graphene. At the chosen ethylene exposure temperature, graphene growth is self-limiting to a single graphene layer that overgrows substrate steps, like a continuous carpet [60].

Sm and Dy were deposited from high purity rods (99.9%) heated by electron bombardment. The rods have been degassed for about one month to obtain a pressure $p = 7 \times 10^{-11}$ mbar during deposition. The deposition flux for Sm was set to 5.5×10^{-4} ML/s for the first UHV setup and 2.8×10^{-4} ML s^{-1} for the second. For Dy, the deposition flux used was 2.4×10^{-4} ML s^{-1} for the first system and 2.7×10^{-5} ML s^{-1} for the second. In the first setup, the evaporation flux calibration has been performed on samples grown at 280 K (520 K) for an amount of Sm (Dy) corresponding to 30%–50% of the surface. Both elements intercalate and form single layer patches. For the Sm (Dy) packing, we assume a 2×2 structure with respect to the graphene lattice, similar to what has been reported for intercalated Eu on gr/Ir(111) [61, 62]. In the second setup, the

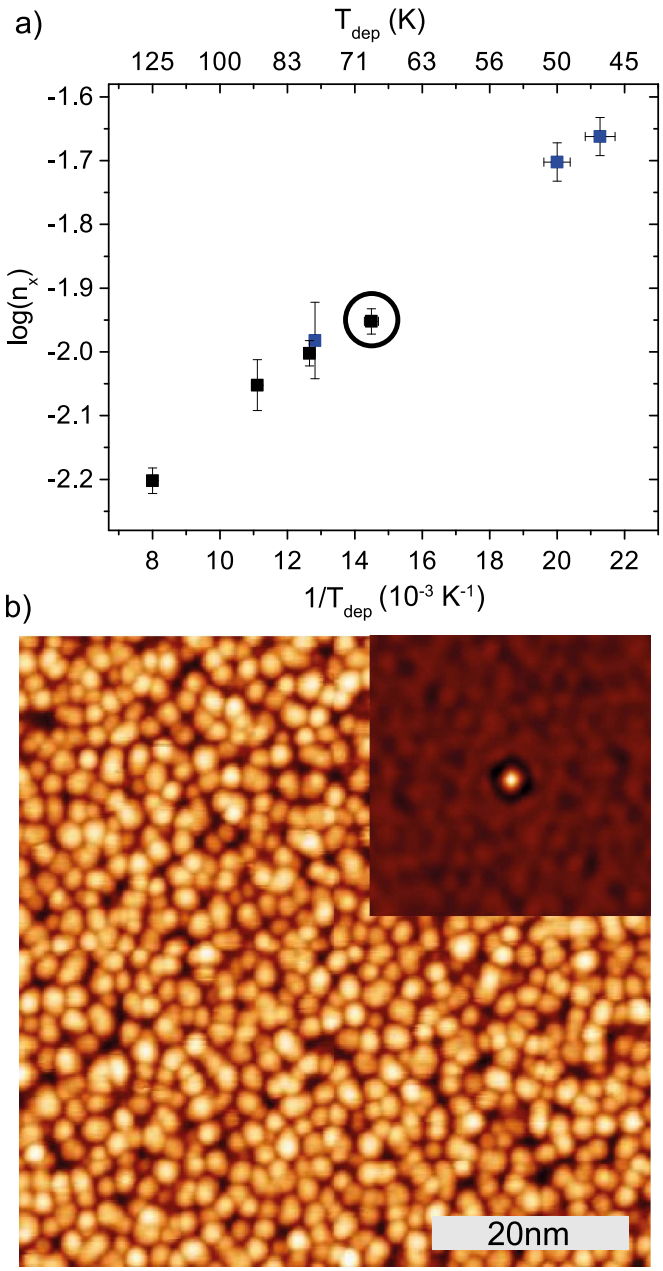

Figure 4. (a) Arrhenius plot of Dy cluster density n_x for $\Theta_{Dy} = 0.07$ ML as a function of T_{dep}. (b) STM image for $T_{dep} = 70$ K ($V_t = +1.0$ V, $I_t = 100$ pA). At this deposition temperature the cluster density is close to the moiré cell density. Inset: 2D-ACF of the image in (b), indicating short-range order.

evaporation flux calibration has been performed by depositing about 1% of ML of Sm (Dy) at 10 K on gr/Ir(111) and by counting the number of deposited atoms. Taking into account the evaporation source stability over time and, for the first setup, the imprecision due to tip convolution effects in the covered-area evaluation, we estimate a 10% error on the coverages given in the text. All STM images were recorded in constant current mode. In order to avoid tip-induced cluster displacement consequences of the weak Sm–graphene bond, we employed tunnel parameters ($R_t \geqslant 20$ GΩ), ensuring a large tip–sample separation. Samples were cooled down right after each deposition to avoid cluster diffusion while setting up the STM. The STM data were processed using a freeware image processing software [63] and our home-written software.

The measured size distributions are strongly affected by tip convolution effects and the corrugated graphene background, also hindering the determination of the 3D cluster shape. For the evaluation of the cluster size, we therefore considered only those pixels corresponding to an apparent height larger than half the height of single layer clusters. The associated pixels are multiplied by the number of layers, which corresponds to the assumption of cylindrical-shaped clusters.

References

[1] Meiwes-Broer K-H 2000 Electronic level structure of metal clusters at surfaces *Metal Clusters at Surfaces: Structure, Quantum Properties, Physical Chemistry* ed K-H Meiwes-Broer (Heidelberg: Springer) pp 151–73
[2] Brune H 1998 Microscopic view of epitaxial metal growth: nucleation and aggregation *Surf. Sci. Rep.* **31** 121
[3] Voigtländer B, Meyer G and Amer N M 1991 Epitaxial growth of thin magnetic cobalt films on Au(111) studied by scanning tunneling microscopy *Phys. Rev.* B **44** 10354–7
[4] Brune H, Giovannini M, Bromann K and Kern K 1998 Self-organized growth of nanostructure arrays on strain-relief patterns *Nature* **394** 451–3
[5] Li J-L, Jia J-F, Liang X-J, Liu X, Wang J-Z, Xue Q-K, Li Z-Q, Tse J S, Zhang Z and Zhang S B 2002 Spontaneous assembly of perfectly ordered identical-size nanocluster arrays *Phys. Rev. Lett.* **88** 066101
[6] Rousset S, Repain V, Baudot G, Garreau Y and Lecoeur J 2003 Self-ordering of Au(111) vicinal surfaces and application to nanostructure organized growth *J. Phys. Condens. Matter* **15** S3363
[7] Degen S, Becker C and Wandelt K 2004 Thin alumina films on $Ni_3Al(111)$: A template for nanostructured Pd cluster growth *Faraday Discuss.* **125** 343–56
[8] Weiss N *et al* 2005 Uniform magnetic properties for an ultrahigh-density lattice of noninteracting Co nanostructures *Phys. Rev. Lett.* **95** 157204
[9] N'Diaye A T, Bleikamp S, Feibelman P J and Michely T 2006 Two-dimensional Ir cluster lattice on a graphene Moiré on Ir(111) *Phys. Rev. Lett.* **97** 215501
[10] Brihuega I, Michaelis C H, Zhang J, Bose S, Sessi V, Honolka J, Schneider M A, Enders A and Kern K 2008 Electronic decoupling and templating of Co nanocluster arrays on the boron nitride nanomesh *Surf. Sci.* **602** L95–9
[11] N'Diaye A T, Gerber T, Busse C, Mysliveček J, Coraux J and Michely T 2009 A versatile fabrication method for cluster superlattices *New J. Phys.* **11** 103045
[12] Natterer F D, Rusponi S, Papagno M, Carbone C and Brune H 2012 Optimizing long-range order, band gap, and group velocities for graphene on close-packed metal surfaces *J. Phys. Condens. Matter* **24** 314203
[13] Pivetta M, Pacchioni G E, Schlickum U, Barth J V and Brune H 2013 Formation of fe cluster superlattice in a metal-organic quantum-box network *Phys. Rev. Lett.* **110** 086102
[14] Schumacher S 2014 Structure, magnetism, and binding of novel two-dimensional materials: Europium-intercalated graphene, cluster lattices, and polar oxide bilayers *PhD Thesis* Universität zu Köln
[15] Cavallin A *et al* 2014 Magnetism and morphology of Co nanocluster superlattices on $GdAu_2$/Au(111)-(13 $\times$13) *Phys. Rev.* B **90** 235419
[16] Aït-Mansour K, Brune H, Passerone D, Schmid M, Xiao W, Ruffieux P, Buchsbaum A, Varga P, Fasel R and Gröning O 2012 Interface-confined mixing and buried partial dislocations for Ag bilayer on Pt(111) *Phys. Rev.* B **86** 085404
[17] Takayanagi K, Tanishiro Y, Takahashi S and Takahashi M 1985 Structure analysis of Si(111)-7 $\times$ 7 reconstructed surface by transmission electron diffraction *Surf. Sci.* **164** 367–92
[18] Jia J, Wang J-Z, Liu X, Xue Q-K, Li Z-Q, Kawazoe Y and Zhang S B 2002 Artificial nanocluster crystal: Lattice of identical Al clusters *Appl. Phys. Lett.* **80** 3186–8
[19] Wang J-Z, Jia J-F, Xiong Z-H and Xue Q-K 2008 Spontaneous formation of Mn nanocluster arrays on a Si(111)-7 $\times$ 7 surface observed with STM *Phys. Rev.* B **78** 045424
[20] Wöll C, Chiang S, Wilson R J and Lippel P H 1989 Determination of atom positions at stacking-fault dislocations on Au(111) by scanning tunneling microscopy *Phys. Rev.* B **39** 7988–91
[21] Barth J V, Brune H, Ertl G and Behm R J 1990 Scanning tunneling microscopy observations on the reconstructed Au(111) surface: Atomic structure, long-range superstructure, rotational domains, and surface defects *Phys. Rev.* B **42** 9307–18
[22] Sicot M, Bouvron S, Zander O, Rüdiger U, Dedkov Y S and Fonin M 2010 Nucleation and growth of nickel nanoclusters on graphene Moiré on Rh(111) *Appl. Phys. Lett.* **96** 093115
[23] Engstfeld A K, Beckord S, Lorenz C D and Behm R J 2012 Growth of PtRu clusters on Ru(0001)-supported monolayer graphene films *Chem. Phys. Chem.* **13** 3313–9
[24] Berner S *et al* 2007 Boron nitride nanomesh: Functionality from a corrugated monolayer *Angew. Chem. Int. Ed.* **46** 5115–9
[25] Buluschek P 2007 Submonolayer growth of cobalt on metallic and insulating surfaces studied by scanning tunneling microscopy and kinetic Monte-Carlo simulations *PhD Thesis* École Polytechnique Fédérale de Lausanne (EPFL)
[26] Schmid M, Kresse G, Buchsbaum A, Napetschnig E, Gritschneder S, Reichling M and Varga P 2007 Nanotemplate with holes: Ultrathin alumina on $Ni_3Al(111)$ *Phys. Rev. Lett.* **99** 196104
[27] Skomski R and Sellmyer D 2009 Anisotropy of rare-earth magnets *J. Rare Earths* **27** 675–9
[28] Donati F *et al* 2016 Magnetic remanence in single atoms *Science* **352** 318–21
[29] Rau G *et al* 2014 Reaching the magnetic anisotropy limit of a 3d metal atom *Science* **344** 988
[30] Baumann S *et al* 2015 Origin of perpendicular magnetic anisotropy and large orbital moment in Fe atoms on MgO *Phys. Rev. Lett.* **115** 237202
[31] Singha A, Donati F, Wäckerlin C, Baltic R, Dreiser J, Pivetta M, Rusponi S and Brune H 2016 Magnetic hysteresis in Er Trimers on Cu(111) *Nano Lett.* **16** 3475–81
[32] Steinbrecher M, Sonntag A, Dias M D S, Bouhassoune M, Lounis S, Wiebe J, Wiesendanger R and Khajetoorians A A 2016 Absence of a spin-signature from a single Ho adatom as probed by spin-sensitive tunneling *Nat. Commun.* **7** 10454
[33] Weller D, Moser A, Folks L, Best M E, Lee W, Toney M F, Schwickert M, Thiele J U and Doerner M F 2000 High Ku materials approach to 100 Gbits in^2 *IEEE Trans. Magn.* **36** 10–5
[34] Nozawa T, Sato S and Takahashi R 2009 Vapor-Phase Dehydration of 1,3-butanediol over CeO_2-ZrO_2 Catalysts *Top. Catal.* **52** 609–17
[35] Trillo J and Bernal S 1980 Selectivities of rare earth oxide catalysts for dehydration of butanols *J. Catal.* **66** 184–90
[36] de Klerk A 2014 Contributions of Burtron H. davis to fischer-tropsch refining catalysis: Dehydration as applied to processes for 1-octene production *Top. Catal.* **57** 715–22
[37] Tanabe K, Misono M, Ono Y and Hattori H 1989 *New Solid Acids and Bases Their Catalytic Properties* vol 51 (Amsterdam: Elsevier)
[38] Eric M and Kennedy N W C 1991 *Applied Catalysis* vol 75 (Amsterdam: Elsevier)
[39] Liu X, Wang C-Z, Hupalo M, Lin H-Q, Ho K-M and Tringides M C 2013 Metals on Graphene: interactions, growth morphology, and thermal stability *Crystals* **3** 79
[40] Müller B, Nedelmann L, Fischer B, Brune H and Kern K 1996 Initial stages of Cu epitaxy on Ni(100): Postnucleation and a well-defined transition in critical island size *Phys. Rev.* B **54** 17858–65
[41] N'Diaye A T, Coraux J, Plasa T N, Busse C and Michely T 2008 Structure of epitaxial graphene on Ir(111) *New J. Phys.* **10** 043033

[42] Förster D F, Wehling T O, Schumacher S, Rosch A and Michely T 2012 Phase coexistence of clusters and islands: europium on graphene *New J. Phys.* **14** 023022
[43] Pichler S, Bodnarchuk M I, Kovalenko M V, Yarema M, Springholz G, Talapin D V and Heiss W 2011 Evaluation of ordering in single-component and binary nanocrystal superlattices by analysis of their autocorrelation functions *ACS Nano* **5** 1703–12
[44] Eklund E A, Snyder E J and Williams R 1993 Correlation from randomness: Quantitative analysis of ion-etched graphite surfaces using the scanning tunneling microscope *Surf. Sci.* **285** 157–80
[45] Yang H-N, Zhao Y-P, Chan A, Lu T-M and Wang G-C 1997 Sampling-induced hidden cycles in correlated random rough surfaces *Phys. Rev.* B **56** 4224–32
[46] Rusponi S, Costantini G, Boragno C and Valbusa U 1998 Scaling laws of the ripple morphology on Cu(110) *Phys. Rev. Lett.* **81** 4184–7
[47] Khan N A and Matranga C 2008 Nucleation and growth of Fe and FeO nanoparticles and films on Au(1 1 1) *Surf. Sci.* **602** 932–42
[48] Cullen W and First P 1999 Island shapes and intermixing for submonolayer nickel on Au(111) *Surf. Sci.* **420** 53–64
[49] Baltic R, Pivetta M, Donati F, Wäckerlin C, Singha A, Dreiser J, Rusponi S and Brune H 2016 Superlattice of single atom magnets on graphene *Nano Lett.* **16** 7610–5
[50] Buchsbaum A, De Santis M, Tolentino H C N, Schmid M and Varga P 2010 Highly ordered Pd, Fe, and Co clusters on alumina on $Ni_3Al(111)$ *Phys. Rev.* B **81** 115420
[51] Chambliss D D, Wilson R J and Chiang S 1991 Nucleation of ordered Ni island arrays on Au(111) by surface-lattice dislocations *Phys. Rev. Lett.* **66** 1721–4
[52] Vlaic S, Gragnaniello L, Rusponi S, Cavallin A, Donati F, Dubout Q, Piamonteze C, Dreiser J, Nolting F and Brune H 2014 Interlayer exchange coupling in ordered Fe nanocluster arrays grown on $Al_2O_3/Ni_3Al(111)$ *Phys. Rev.* B **89** 245402
[53] Repain V, Baudot G, Ellmer H and Rousset S 2002 Ordered growth of cobalt nanostructures on a Au(111) vicinal surface: nucleation mechanisms and temperature behavior *Mat. Sci. Eng. B-Solid* **96** 178–87
[54] Lehnert A, Buluschek P, Weiss N, Giesecke J, Treier M, Rusponi S and Brune H 2009 High resolution *in situ* magneto-optic Kerr effect and scanning tunneling microscopy setup with all optical components in UHV *Rev. Sci. Instrum.* **80** 023902
[55] Lai M Y and Wang Y L 2001 Self-organized two-dimensional lattice of magic clusters *Phys. Rev.* B **64** 241404(R)
[56] Knudsen J, Feibelman P J, Gerber T, Grånäs E, Schulte K, Stratmann P, Andersen J N and Michely T 2012 Clusters binding to the graphene moiré on Ir(111): x-ray photoemission compared to density functional calculations *Phys. Rev.* B **85** 035407
[57] Busse C *et al* 2011 Graphene on Ir(111): Physisorption with chemical modulation *Phys. Rev. Lett.* **107** 036101
[58] Liu X, Wang C Z, Hupalo M, Lu W C, Tringides M C, Yao Y X and Ho K M 2012 Metals on graphene: correlation between adatom adsorption behavior and growth morphology *Phys. Chem. Chem. Phys.* **14** 9157–66
[59] Gaisch R, Gimzewski J K, Reihl B, Schlittler R R, Tschudy M and Schneider W D 1992 Low-temperature ultra-high vacuum scanning tunneling microscope *Ultramicroscopy* **42–44** 1621
[60] Coraux J, N'Diaye A T, Busse C and Michely T 2008 Structural coherency of graphene on Ir(111) *Nano Lett.* **8** 565–70
[61] Schumacher S, Förster D F, Rösner M, Wehling T O and Michely T 2013 Strain in epitaxial graphene visualized by intercalation *Phys. Rev. Lett.* **110** 086111
[62] Schumacher S *et al* 2014 Europium underneath graphene on Ir(111): intercalation mechanism, magnetism, and band structure *Phys. Rev.* B **90** 235437
[63] Horcas I, Fernández R, Gómez-Rodríguez J M, Colchero J, Gómez-Herrero J and Baro A M 2007 WSXM: a software for scanning probe microscopy and a tool for nanotechnology *Rev. Sci. Instrum.* **78** 013705